Figure S1: Determination of MT polarity and protofilament architecture in primary neurons.
A. top: 9 nm x-y tomographic slices of a neuronal dendrite containing 4 MTs superimposed with lattice map following STA (Methods). Green indicate high CCC-values, whereas orange and red indicate lower CCC-values. Bottom: missing wedge compensated, denoised cross-section view shows centrally located lumenal particles (x-z slice; arrowheads). **B**. Zoomed in image of the lattice map within the black box in (A) showing different orientations of the subtomograms. **C**. Individually averaged MTs displaying different polarity indicated by plus/minus sign based on the inclinations of the tubulin subunits. **D**. Comparison of CCC-values between flipped and un-flipped data of the reference used to determine MT polarity, with the mean (black dot). Error bar indicate standard error. Statistical significance **p<0.01, obtained by nonparametric Mann-Whitney test. **E**. Subtomogram averages of the neuronal MT at bin4, bin2 and un-binned resolution (bin 1; pixel size 2.24Å). **F**. Fourier Shell Correlation (FSC) plot of the un-binned subtomogram average obtained using 34906 subtomograms from three tomograms.
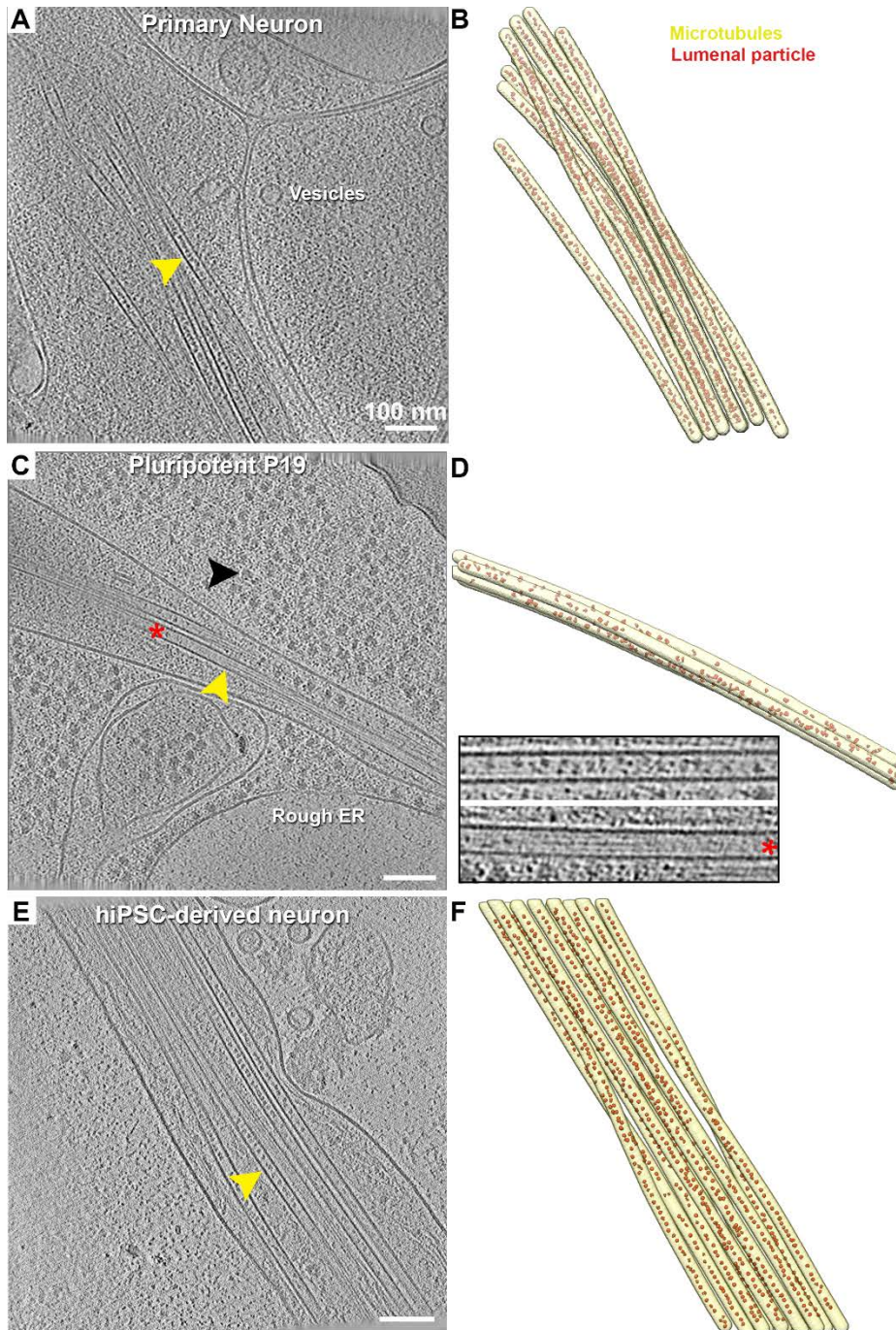
Figure S2: MTs and lumenal particle distribution in different cell types. Tomographic slices and 3D-surface rendering of traced MTs (yellow), along with the detected lumenal particles (red) of indicated cell types: **A**, **B.** Rodent primary neuron, slice thickness 9 nm; **C**, **D.** Pluripotent P19 cell, slice thickness 6.8 nm; Inset: Zoomed in image of an empty MT marked by red star in (C; shown at different orientation) compared to its neighboring MT. **E**, **F.** hiPSC-derived neuronal process, slice thickness 4.25 nm. MTs (yellow arrow), ribosomes (black arrow) and other organelles are indicated in the tomograms.
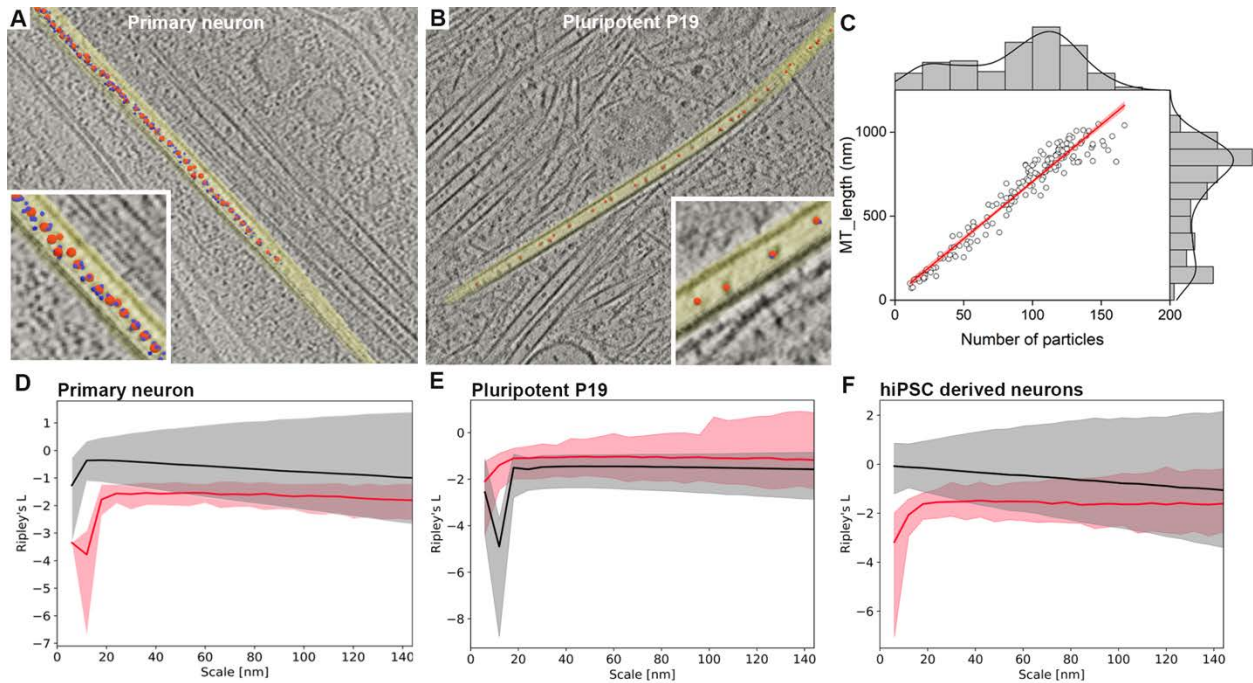
Figure S3: Template-free detection, picking and organization of lumenal particles. A. 9 nm thick tomographic slice of a primary neuronal process. Small blue spheres represent local minima obtained after topological simplifications, big red spheres are the final picking points representing mean shift clustering centers. Inset shows zoomed in image of the same. **B**. 6.8 nm thick tomographic slice of a pluripotent P19 cellular process. Red dots showing detected particles after topological persistence and mean shift clustering. Inset shows zoomed in image. **C**. Linear correlation between MT length and particle number in primary neurons indicating packing ratio of the particles within the lumen. Red line indicates linear fitting with Pearson's r=0.97. **D-F.** Univariate 2nd order Ripley's L showing uniform distribution of lumenal particles within MTs of different cell types. Red and black lines indicate medians of the Ripley's L function for the experimental and simulated random distribution, respectively. Shaded areas define the intervals of confidence [5, 95] %.
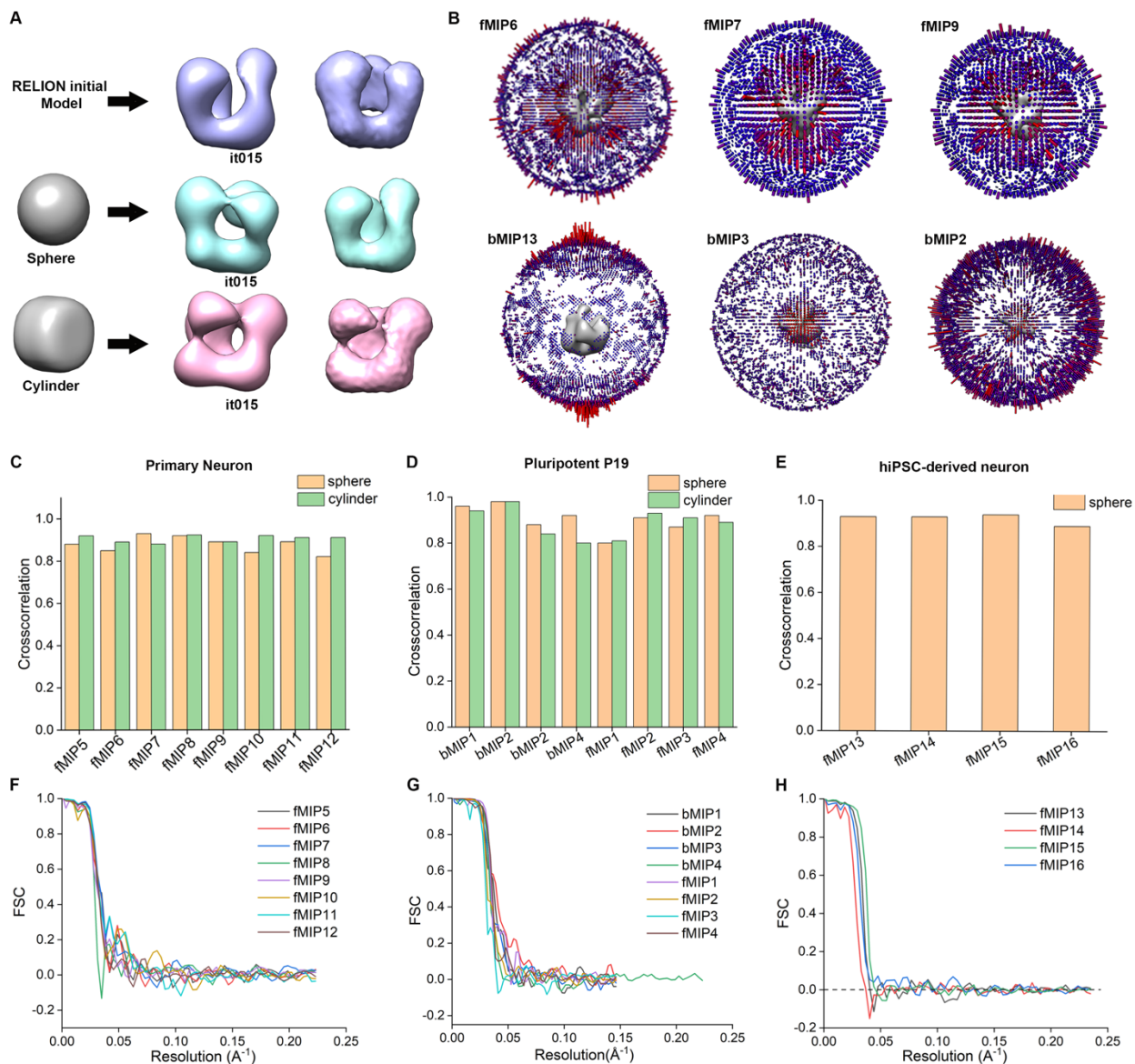
Figure S4: Validation of STA-generated lumenal particle maps from various cell lines. A. A representative example shows evolution of fMIP9 average from various starting models. B. Angular distributions obtained from the averages for representative cases. C-E. Similarity between the averages obtained from the indicated starting models for C) primary neuron, D) pluripotent P19 cells and E) hiPSC-derived neurons, and the corresponding averages obtained from RELION starting model, evaluated using cross-correlation coefficient in Chimera. F-H. FSC curves of the post-processed averages from F) primary neuron, G) pluripotent P19 cells and H) hiPSC-derived neuronal samples.
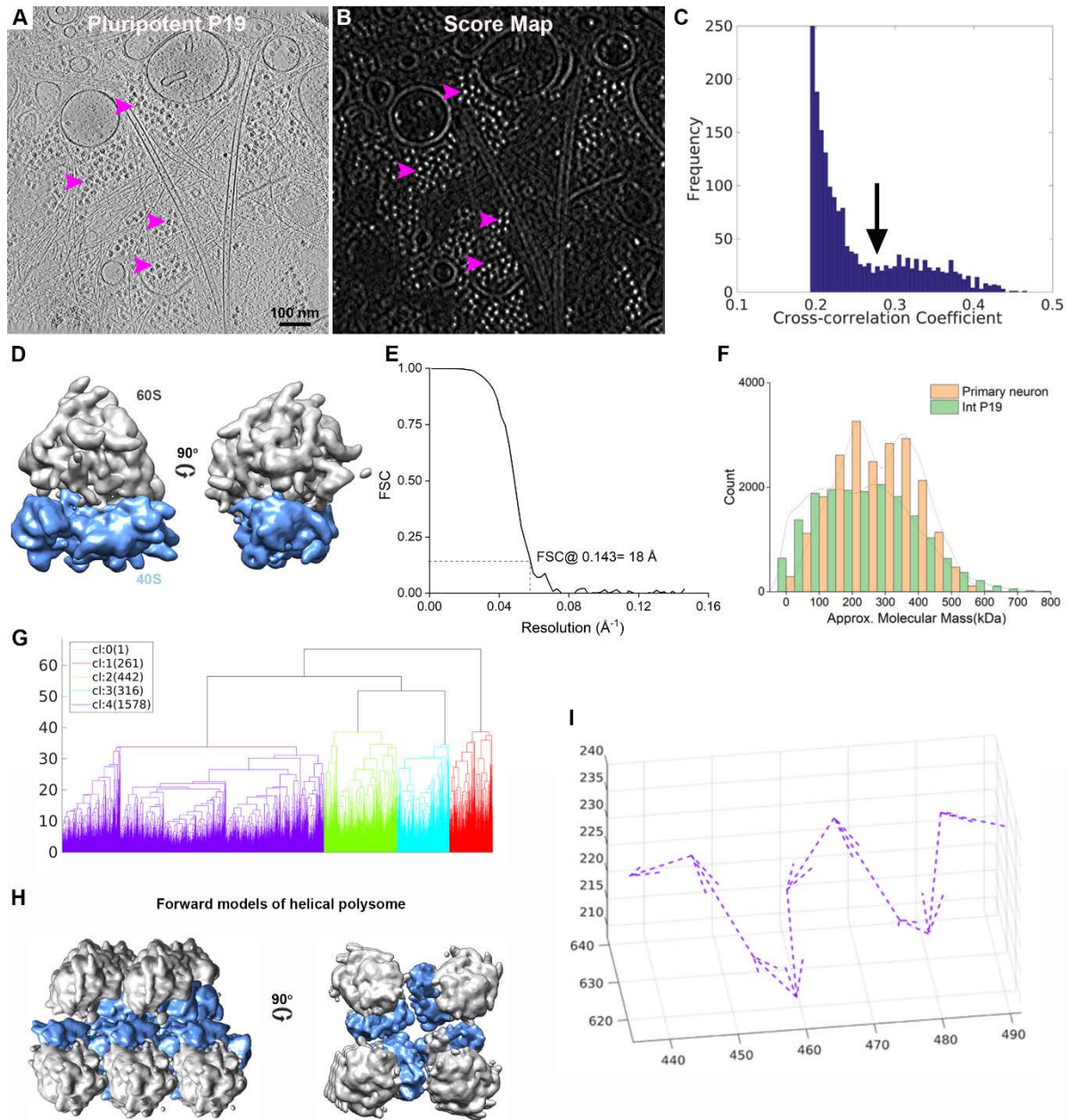
Figure S5: Template matching, STA and organization of cellular ribosomes. A. 6.8 nm tomographic slice of a pluripotent P19 cytoplasm. Examples of ribosomes are indicated by violet arrowheads. **B**. Cross-correlation Score map of the same tomogram following template matching in PyTom. Bright spots indicate high scores. Same ribosome clusters as in A, are indicated. **C**. Histogram of cross-correlation coefficients obtained after template matching. Bimodal distribution indicates false positives and real hits. Black arrow indicates cut-off value chosen to eliminate false positives. **C**. Density map of 80S murine ribosome obtained from 4723 particles by STA in RELION. Large and small subunits are indicated. **E**. FSC curve of the 80S ribosome average obtained after RELION post-processing. **F**. Distribution of approximate mass of the lumenal particles of indicated samples calculated from the corresponding tomograms. Particle mass was measured using isosurface threshold that corresponds to the molecular weight of the 80S ribosome particles present in the same tomograms. Lines indicate fit to the data distribution. **G**.

Hierarchical clustering of transformations of distance matrices calculated from rotations and translations between ribosome pairs. **H**. Representative helical polysome class corresponding to largest cluster (purple) in (G). 60S subunits (gray) face cytosol. **I**. Vector diagram showed longest helical polysome traced. Arrows indicate translations from n to n+1 ribosome. Axis unit is in pixels.
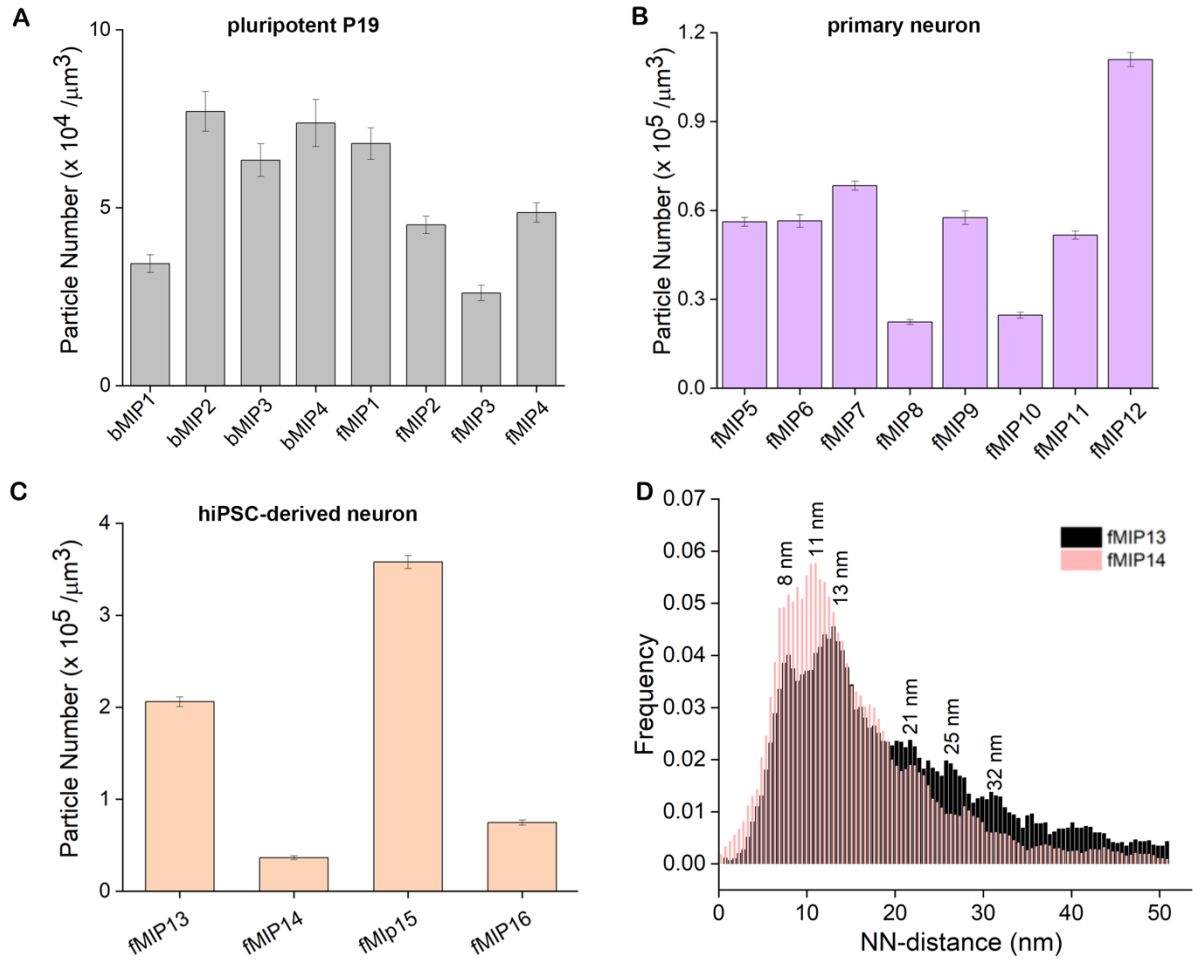
Figure S6: Abundances of the lumenal particle class averages. Concentrations of the various class averages obtained from **A**. pluripotent P19 cells, **B**. primary neuron and **C**. hiPSC-derived neuron. Error bar indicates SEM. **D**. NN-distance distribution of indicated class averages in hiPSC-derived neurons. Major peaks are indicated.
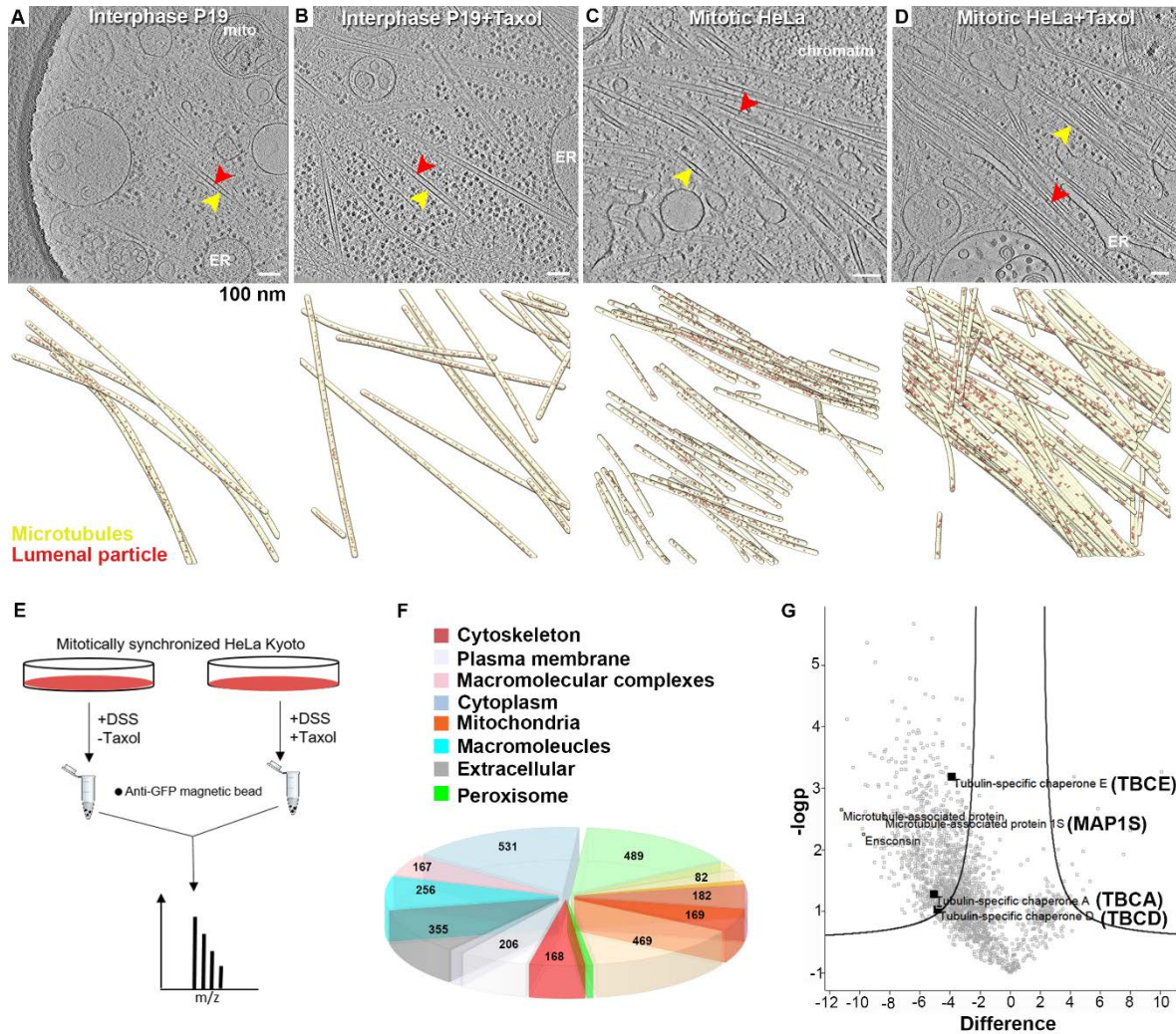
Figure S7. Effect of Taxol and its utilization in AP-MS analysis of MT-interacting proteins in mitotic HeLa cells expressing GFP tagged β–tubulin. Tomographic slices (top row) and 3D-surface rendered MTs (yellow), along with the lumenal particles (red) of indicated cells (bottom row): **A.** pluripotent P19 cells, slice thickness 6.8 nm; **B.** Taxol treated pluripotent P19 cell, slice thickness 6.8 nm; **C.** mitotic HeLa cells, slice thickness 8.4 nm; **D.** Taxol treated mitotic HeLa cells, slice thickness 8.4 nm. **E**. Experimental strategy of identifying lumenal particles from their fold reduction due to Taxol treatment. **F**. Pie chart shows distribution of cellular components based on gene-ontology (GO)-categorization of the affinity purified proteins identified in the Mass spectrometry-based proteomics. Numbers indicate number of protein that belong to each subcategory. **G**. Volcano plot showing fold enrichment of different proteins between control and Taxol treated HeLa cell samples. Some of the proteins that showed significant fold (p<0.05) change are highlighted (black box).
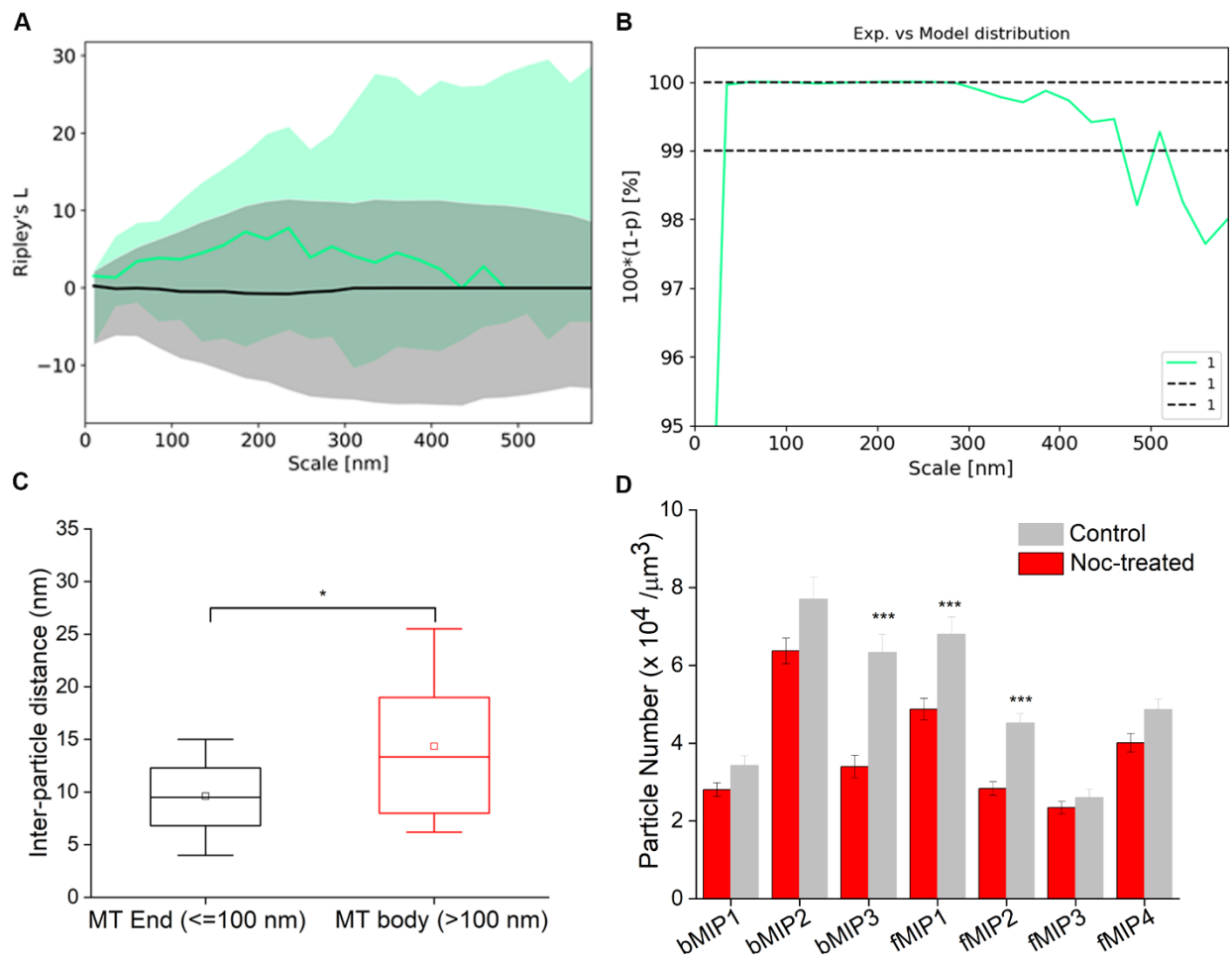
Figure S8: Clustering of particles at the MT plus ends in Noc-treated pluripotent P19 cells.
A. Experimental (green) vs. random simulated null-model (black). Lines represent the median and shaded areas the interval of confidence [5, 95]%. **B**. One sided Welch test for comparison between the experimental mean (green line) and the simulated one for every scale. Black dashed lines demarcated region indicate area of 99% significance. At a distance >200 nm, significance drops indicating clustering (higher density than random null-model) only occurs at the plus end. **C**. Boxplot shows distance between the particles located within 100 nm from the MT end (black box) and further away (red box). Line indicate median and small rectangle denotes mean value. N=5, statistical significance by two sample t-test, P<0.05. **D**. Concentrations of the indicated class averages in control and Noc-treated undifferentiated P19 cells. Error bar indicates SEM. Statistical significance ***p<0.001, obtained by two-sample t-test.

Table S1: Summary of the data sets from different cell types used for STA*.

	Murine P19 cells	Human iPSC derived neuron	Rat primary neuron	Global resolution FSC @0.143 (Å)
#VPP tomograms	46	8	-	-
#Defocus tomograms	35	-	60	-
#subtomograms	44,944	8635	51,734	-
#bMIP1 subtomograms	4411	-	-	21.05
#bMIP2 subtomograms	4466	-	-	16.69
#bMIP3 subtomograms	3224	-	-	21.46
#bMIP4 subtomograms	1519	-	-	24.45
#fMIP1 subtomograms	3825	-	-	20.12
#fMIP2 subtomograms	2536	-	-	23.87
#fMIP3 subtomograms	1653	-	-	26.39
#fMIP4 subtomograms	3060	-	-	25.91
#fMIP5 subtomograms	-	-	2567	25.25
#fMIP6 subtomograms	-	-	2580	26.18
#fMIP7 subtomograms	-	-	3126	20.92
#fMIP8 subtomograms	-	-	1021	32.26
#fMIP9 subtomograms	-	-	2621	22.03
#fMIP10 subtomograms	-	-	1126	26.81
#fMIP11 subtomograms	-	-	2362	27.55
#fMIP12 subtomograms	-	-	5071	26.60
#fMIP13 subtomograms	-	2151	-	26.46
#fMIP14 subtomograms	-	380	-	30.86
#fMIP15 subtomograms	-	3738	-	24.51
#fMIP16 subtomograms	-	779	-	27.1
#80S Ribosome subtomograms	4723	-	-	17.27
# MT subtomograms			34906	8.19

*In case of pluripotent and differentiated P19 cells, both VPP and defocus data were obtained and processed separately.

Supplemental video title and legends

Movie S1: Cryo-tomogram of a primary hippocampal neuronal process. Related to Figure 1A, S1A. Tomographic slices of primary neuronal showing the ultrastructure of the MT cytoskeleton. MTs (yellow), lumenal particles (red) are visible and correspond to the Fig. 1A and Fig.S1A.

Movie S2: Cryo-tomogram of a pluripotent P19 cell. Related to Figure 1D. Tomographic slices of an intact P19 cellular process showing the ultrastructure of the cytoplasm containing MTs. Color coding, MT: yellow and lumenal particles: red.

Movie S3: Cryo-tomogram of a hiPSC-derived neuron. Related to Figure 1D. Tomographic slices of a hiPSC-derived neuronal process showing the ultrastructure of MTs. Color coding, MT: yellow and lumenal particles: red.

Movie S4: Cryo-tomogram of a Taxol-treated pluripotent P19 cell. Related to Figure 3A. Tomographic slices of a Taxol-treated pluripotent P19 cellular process showing the ultrastructure of the cytoplasm containing MTs. Color coding, MT: yellow and lumenal particles: red.

Movie S5: Cryo-tomogram of Noc-treated pluripotent P19 cell. Related to Figure 7G. Tomographic slices of an intact pluripotent P19 cellular process showing the freshly polymerized MTs after Nocodazole washout. Color coding, MT: yellow and lumenal particles: red.